nature communications

Article

https://doi.org/10.1038/s41467-023-38336-5

Selective conversion of CO_2 to isobutane-enriched C_4 alkanes over $InZrO_x$-Beta composite catalyst

Received: 10 November 2022

Accepted: 25 April 2023

Published online: 06 May 2023

Check for updates

Han Wang[1,2,3], Sheng Fan[1,2,3], Shujia Guo[1,2], Sen Wang[1] ✉, Zhangfeng Qin[1] ✉, Mei Dong[1], Huaqing Zhu[1], Weibin Fan[1] & Jianguo Wang[1,2] ✉

Direct conversion of CO_2 to a single specific hydrocarbon with high selectivity is extremely attractive but very challenging. Herein, by employing an $InZrO_x$-Beta composite catalyst in the CO_2 hydrogenation, a high selectivity of 53.4% to butane is achieved in hydrocarbons (CO free) under 315 °C and 3.0 MPa, at a CO_2 conversion of 20.4%. Various characterizations and DFT calculation reveal that the generation of methanol-related intermediates by CO_2 hydrogenation is closely related to the surface oxygen vacancies of $InZrO_x$, which can be tuned through modulating the preparation methods. In contrast, the three-dimensional 12-ring channels of H-Beta conduces to forming higher methylbenzenes and methylnaphthalenes containing isopropyl side-chain, which favors the transformation of methanol-related intermediates to butane through alkyl side-chain elimination and subsequent methylation and hydrogenation. Moreover, the catalytic stability of $InZrO_x$-Beta in the CO_2 hydrogenation is considerably improved by a surface silica protection strategy which can effectively inhibit the indium migration.

The hydrogenation of CO_2 to hydrocarbons using green hydrogen is now considered a practical process in tackling the globe warming caused by excessive emission of greenhouse gases[1–3] as well as in recycling CO_2 as a carbon feedstock to produce value-added chemicals[4–8]. In this regard, the conversion of CO_2 into bulk chemicals including light olefins[9–12] and aromatics[13–16] has attracted special attention. Two routes are now proposed for the CO_2 hydrogenation, viz., the modified Fischer-Tropsch synthesis (FTS) one using Fe- or Co-based catalysts[17–21] and the methanol-mediated one over a composite catalyst consisting of metal oxides and zeotypes (OX-ZEO)[11,22]. As the FTS route keeps to the Anderson-Schultz-Flory (ASF) rule for the product distribution, a wide spectrum of hydrocarbons are produced. In contrast, the selectivity to the target olefin and aromatic products can be considerably improved by using the OX-ZEO composite catalyst via the methanol-mediated route which dispenses with the ASF rule[16,23].

Great progress has been made in the hydrogenation of CO_2 to C_2–C_3 alkenes/alkanes in recent years. Through the regulation of surface electronic structure of metal oxides and acidic properties of zeotypes, a high selectivity to ethene (ca. 70%)[24], propene + butene (ca. 65%)[25], or propane (ca. 70%)[26] was achieved for the CO_2 hydrogenation. Nonetheless, it is very challenging to achieve a high selectivity to a defined hydrocarbon (in particular a relatively long chain one) through the CO_2 hydrogenation, due to the chemical inertia of CO_2 and the complexity of C–C coupling reactions. For example, the selective hydrogenation of CO_2 into C_{4+} hydrocarbons is rarely reported[27], although the C_{4+} hydrocarbons are highly valuable as clean fuel and solvents. In this regard, butane is widely used as fuel (liquefied gas), refrigerant, spray, and feedstock in chemical synthesis. Traditionally, butane is obtained from petroleum cracking[28]. The direct conversion of CO_2 to butane under mild reaction conditions may provide a new strategy for the renewable

[1]State Key Laboratory of Coal Conversion, Institute of Coal Chemistry, Chinese Academy of Sciences, P.O. Box 165 Taiyuan, Shanxi 030001, P. R. China. [2]University of Chinese Academy of Sciences, Beijing 100049, P. R. China. [3]These authors contributed equally: Han Wang, Sheng Fan.
✉e-mail: wangsen@sxicc.ac.cn; qzhf@sxicc.ac.cn; iccjgw@sxicc.ac.cn

production of C_{4+} chemicals. Unfortunately, current reported catalyst in general gave a rather low selectivity to butane (<30%)[29]. In addition, to improve the practicability of CO_2 hydrogenation to demanded hydrocarbons, the formation of CH_4 (from CO_2 methanation) and CO (from reverse water-gas shift, RWGS) should also be suppressed to the utmost.

For the CO_2 hydrogenation over a bifunctional OX-ZEO catalyst, first, the oxide moiety should be highly effective in building methanol-related intermediate. In_2O_3 is a promising catalyst component for the CO_2 hydrogenation to methanol, showing high activity at a high temperature of 280–330 °C[30–32]. To suppress the formation of CH_4 and CO, various dopants were used to regulate the crystal structure and surface electronic properties of In_2O_3[33–36]; among them, doping Zr into In_2O_3 proved to be rather effective. Frei and co-workers observed that Zr was able to increase the concentration of surface oxygen vacancies of In_2O_3, which could then promote the adsorption and activation of CO_2 and raise the selectivity to methanol[37]. Chen and co-workers found that the interfacial interaction between In_2O_3 and ZrO_2 was favorable to the formation of methanol[38]. Similarly, a high methanol space time yield (STY) was observed over $InZrO_x$ in the CO_2 hydrogenation[39,40].

Next, the zeotype moiety must work in close cooperation with the oxide moiety to achieve a high yield of specific hydrocarbon. The zeotype moiety is responsible for the successive transformation of the methanol-related intermediates generated on the oxide moiety into hydrocarbons on the acid sites in the confined interspace[41,42]. Naturally, the distribution of products on the OX-ZEO catalysts is closely related to the topology framework and acidity of the zeotype moiety. Various composite catalysts like $InZrO_x$/SSZ-13[26], In_2O_3/SAPO-34[35], and In_2O_3/ZSM-5[43] were used in the CO_2 hydrogenation, which were selective to alkanes (C_2^0–C_4^0), light olefins ($C_2^=$–$C_4^=$), and liquid fuels, respectively. It implies that higher alkanes/alkenes like butane may request the zeotype moiety a relative large pore channel such as Beta, which can accommodate large reaction intermediates and allow the quick diffusion of large molecular products. In addition, the facile synthesis of Beta zeolite with a wide range of Si/Al ratio makes it attractive as a catalyst component in the conversion of methanol[44]. It is then expected that a bifunctional catalyst composed of Zr-doped In_2O_3 and H-Beta may give a high yield of C_4 hydrocarbons for the CO_2 hydrogenation. However, we have seldom noticed such reports in this regard, despite that the In-based catalysts have been widely used in the CO_2 hydrogenation to alcohols and light alkene and alkane mixtures. In addition, Wang and co-workers reported recently that the indium species in the oxide moiety would continuously run off during the reaction process, resulting in a rapid poisoning of the acid sites on the zeotype moiety[45], which may also inhibit the application of In_2O_3 in the bifunctional catalyst in practice for the CO_2 hydrogenation to hydrocarbons.

Herein, a bifunctional composite catalyst consisting of $InZrO_x$ oxide and H-Beta zeolite was designed and employed in the hydrogenation of CO_2; a high selectivity of 53.4% to butane in all hydrocarbons (CO free) is achieved under 315 °C, 3.0 MPa, and a space velocity of 1200 mL g^{-1} h^{-1} (H_2/CO_2 = 3), at a CO_2 conversion of 20.4% and a selectivity of only about 2% to CH_4. Combining with various characterization measures and density-functional theory (DFT) calculation, it is revealed that the high selectivity to butane originates from the hydrocarbon pool (HCP) in the H-Beta zeolite filled with bulkier methylbenzenes and methylnaphthalenes, via an alkyl side-chain intermediate. Moreover, a surface silica protection strategy was developed, which can effectively inhibit the phase separation of $InZrO_x$ oxide and the migration of In species into the H-Beta zeolite and then considerably improve the catalytic stability of $InZrO_x$-Beta in the CO_2 hydrogenation. These results pave a way for the design of stable In-based catalyst in the CO_2 hydrogenation to a specific hydrocarbon product.

Results

Textural and structural properties of $InZrO_x$

Supplementary Table 1 and Supplementary Fig. 1 give the textural properties of the $InZrO_x$ oxides prepared by different methods determined by N_2 sorption. Apparently, the surface area of three $InZrO_x$ oxides decreases in the order of $InZrO_x$(CP) (73 m^2 g^{-1}) > $InZrO_x$(SG) (59 m^2 g^{-1}) > $InZrO_x$(HT) (41 m^2 g^{-1}); in addition, $InZrO_x$(CP) also displays much larger mesopore volume (0.31 cm^3 g^{-1}) than $InZrO_x$(SG) (0.07 cm^3 g^{-1}) and $InZrO_x$(HT) (0.15 cm^3 g^{-1}).

Figure 1 shows the XRD patterns and TEM images of the $InZrO_x$ oxides prepared by different methods. In the HRTEM images, the (211) and (222) crystal facets, with a lattice spacing of 0.405–0.410 and 0.290–0.291 nm, respectively, are resolved for three $InZrO_x$ oxides (Fig. 1a–c)[10]. Five diffraction peaks at 21.5°, 30.6°, 35.5°, 51.0°, and 60.7° are observed for all three $InZrO_x$ oxides (Fig. 1d), corresponding to the (211), (222), (400), (440) and (622) crystal facets of cubic In_2O_3, respectively (JCPDS PDF#06-0416)[42]. Furthermore, the TEM images shown in Supplementary Fig. 2 illustrated that all three $InZrO_x$ oxides are aggregates of spherical nano particles (NPs), with a mean size of 9.76 nm for $InZrO_x$(CP) (prepared by co-precipitation), 9.19 nm for $InZrO_x$(SG) (by sol-gel method), and 25.18 nm for $InZrO_x$(HT) (by hydrothermal method). The STEM-EDX elemental mapping results indicate that the In, Zr, and O elements are uniformly dispersed with each other in the $InZrO_x$ oxides (Fig. 1e–i and Supplementary Figs. 3, 4).

The surface electronic state of various $InZrO_x$ oxides was analyzed by XPS, as shown in Supplementary Fig. 5. The peaks at 444.4 and 451.8 eV in the In 3*d* XPS spectra correspond to $3d_{5/2}$ and $3d_{3/2}$ of In^{3+}, respectively, while those at 182.4 and 184.8 eV in the Zr 3*d* XPS spectra are assigned to $3d_{5/2}$ and $3d_{3/2}$ of Zr^{4+}, respectively. The O 1*s* XPS spectra reveal three oxygen species in the $InZrO_x$ oxides (Fig. 2a)[46]; the peaks at 532.6, 531.4, and 529.9 eV are ascribed to the surface hydroxyl groups (–OH), oxygen around the vacancies (O_{defect}), and lattice oxygen ($O_{lattice}$), respectively. The deconvolution results indicate that the fraction of surface oxygen around the vacancies (representing the abundance of oxygen vacancies) for three $InZrO_x$ oxides decreases in the order of $InZrO_x$(CP) (36.15%) > $InZrO_x$(SG) (32.39%) > $InZrO_x$(HT) (27.65%). In addition, the same sequence of three oxides by the surface oxygen vacancy concentration is manifested by the in situ O 1*s* XPS results (Supplementary Fig. 6), viz., $InZrO_x$(CP) (43.47%) > $InZrO_x$(SG) (36.75%) > $InZrO_x$(HT) (31.76%). The in situ O 1*s* XPS gives higher surface oxygen vacancy concentrations than the ex situ one, which is ascribed to the fact that more surface oxygen defects are formed due to the elimination of certain surface oxygen atoms by reduction in the in situ H_2-containing atmosphere, in agreement with previous works[24,47].

Figure 2b shows the H_2-TPR profiles of various $InZrO_x$ oxides. The high temperature peak (centered around 650 °C) is attributed to the reduction of bulk In_2O_3, whereas the low temperature one (150–250 °C) is due to the annihilation of surface oxygen from In_2O_3[47]. Apparently, $InZrO_x$(CP) displays a more intense H_2 consumption peak (19 μmol g^{-1}) attributed to the removal of surface oxygen at a lower temperature (160 °C), in comparison with $InZrO_x$(SG) (18 μmol g^{-1}, at 180 °C) and $InZrO_x$(HT) (16 μmol g^{-1}, at 220 °C), indicating that $InZrO_x$(CP) has more surface defects (oxygen vacancies), agreeing well with above O 1*s* XPS results. The Rietveld refinement of the in situ XRD patterns (Supplementary Fig. 7) indicates that the cell volume of $InZrO_x$ decreases after H_2 reduction, due to the release of surface oxygen atoms[47]. Interestingly, as shown in Fig. 2c, $InZrO_x$(CP) also displays the highest cell shrinkage ratio than $InZrO_x$(SG) and $InZrO_x$(HT), according well with the more surface defects of $InZrO_x$(CP). Moreover, since the onset temperature for the reduction of bulk In_2O_3 to metallic indium species is only around 315 °C, it is conceivable that certain metallic indium species may be generated on the surface of $InZrO_x$ oxide during the reduction and subsequent reaction processes. These metallic indium species may easily migrate

https://doi.org/10.1038/s41467-023-38336-5

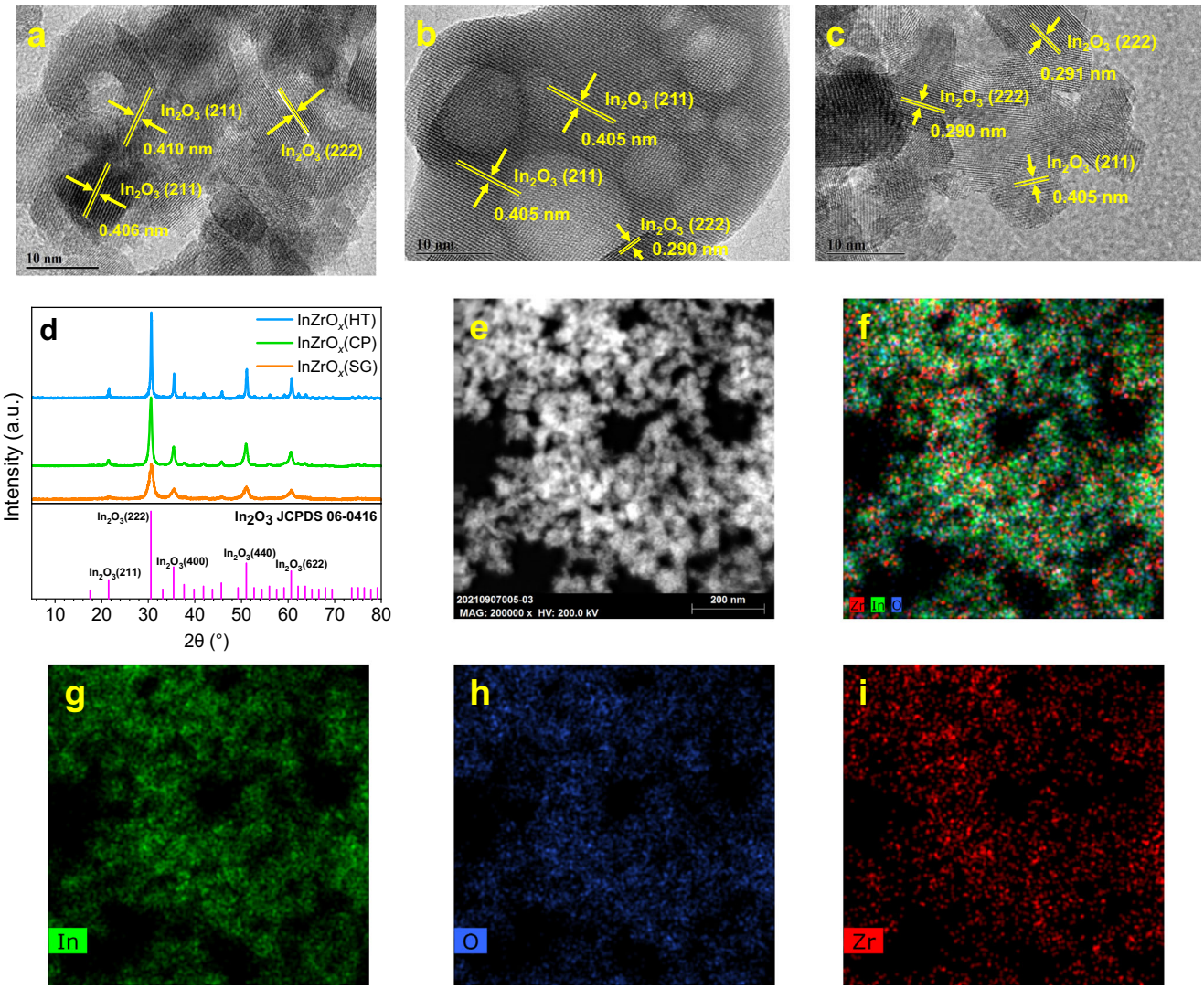

Fig. 1 | Structure of various $InZrO_x$ oxides. a–c HRTEM images of $InZrO_x$(CP) (**a**), $InZrO_x$(HT) (**b**), and $InZrO_x$(SG) (**c**); **d** XRD patterns of $InZrO_x$ prepared by different methods; **e–i** STEM-EDX elemental mapping of $InZrO_x$(CP).

to the zeolite moiety and then poison the acid sites of zeolite component[45,47]; this will be discussed in detail in the following section.

Figure 2d displays the CO_2-TPD profiles of various $InZrO_x$ oxides. The peak below 150 °C represents the physical adsorption of CO_2, whereas that at above 300 °C is ascribed to the chemical adsorption of CO_2 on the surface oxygen defects[42]. As expected, $InZrO_x$(CP) exhibits larger CO_2 desorption amount at above 300 °C, followed by $InZrO_x$(SG) and $InZrO_x$(HT). It further evinces that CO_2 adsorption is enhanced on $InZrO_x$(CP) (prepared by co-precipitation) with abundant oxygen vacancies.

Properties of H-Beta zeolites

As illustrated in Supplementary Fig. 8a, b, the H-Beta, H-SSZ-13 and USY zeolites used in this work have a typical BEA, CHA and FAU topological framework, respectively, with high crystallinity. N_2 sorption results (Supplementary Fig. 8c and Supplementary Table 2) indicate that various H-Beta zeolites with different Si/Al ratios (20–100) are similar in their textural properties. The SEM images shown in Supplementary Fig. 9 display that the H-Beta zeolites has a particle size of around 1 μm. In contrast, the NH_3-TPD results given in Supplementary Table 2 and Supplementary Fig. 8d indicate that both the weak acid and strong acid contents of H-Beta decrease with the increase of the Si/Al ratio.

Catalytic performance of $InZrO_x$-Beta in the CO_2 hydrogenation

The $InZrO_x$ oxides alone were first tested for the hydrogenation of CO_2 under 315 °C, 3.0 MPa, and with a space velocity (SV) of 2400 mL g^{-1} h^{-1} and H_2/CO_2 ratio of 3 in the feed. As shown in Supplementary Fig. 10, $InZrO_x$(CP) prepared by co-precipitation exhibits a higher CO_2 conversion (18.7%) and a higher methanol space time yield (STY) (0.012 mol kg^{-1} h^{-1}) than $InZrO_x$(SG) prepared by sol-gel method (17.3% and 0.011 mol kg^{-1} h^{-1}, respectively) and $InZrO_x$(HT) by hydrothermal method (11.2% and 0.003 mol kg^{-1} h^{-1}, respectively).

Next, the catalytic performance of granule-mixed bifunctional $InZrO_x$-Beta catalyst (0.3 g $InZrO_x$ + 0.3 g H-Beta) was evaluated in the hydrogenation of CO_2 under 315 °C, 3.0 MPa, a SV of 1200 mL g^{-1} h^{-1}, and an H_2/CO_2 ratio of 3 in the feed. As shown in Fig. 3a, over $InZrO_x$-Beta(40), butane is the dominant hydrocarbon product. In particular, $InZrO_x$(CP)-Beta(40) exhibits a selectivity of 53.4% to butane in the hydrocarbon products, at a CO_2 conversion of 20.4% and a selectivity of 54.9% to CO. In contrast, over $InZrO_x$(SG)-Beta(40), the selectivity to butane in the hydrocarbon products, CO_2 conversion, and selectivity to CO are 52.9%, 18.7%, and 53.0%, respectively, whereas over $InZrO_x$(HT)-Beta(40), the CO_2 conversion decreases to 12.6%, whilst the selectivity to butane decreases to 34.7%, accompanied by the formation of more C_2–C_3 components. It seems that $InZrO_x$(CP) with abundant oxygen vacancies exhibits high activity in the CO_2

https://doi.org/10.1038/s41467-023-38336-5

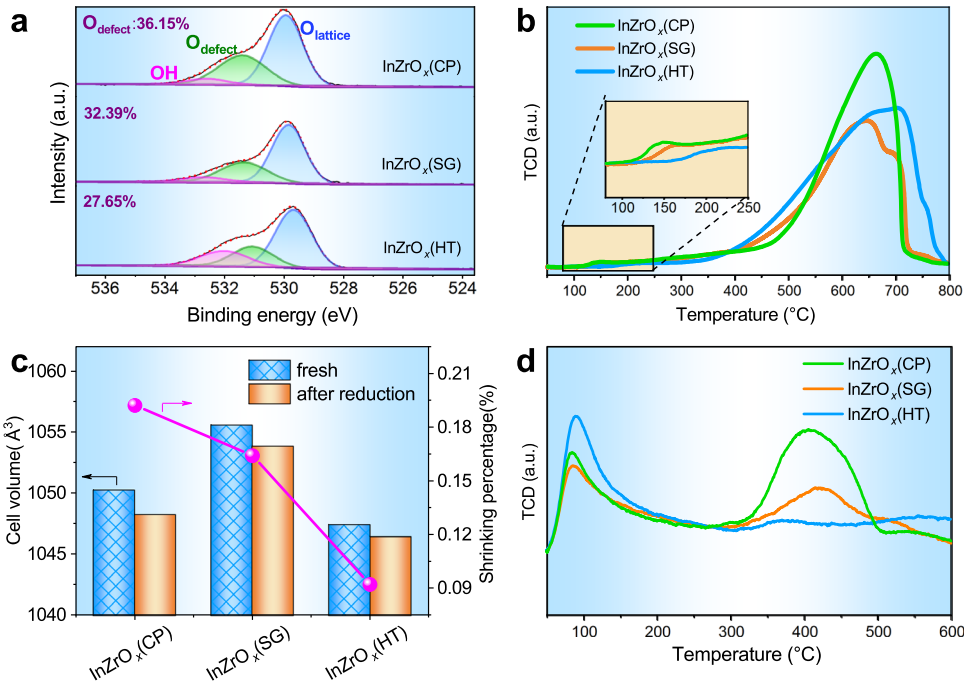

Fig. 2 | Surface electronic state and reduction behavior of $InZrO_x$. **a** O 1*s* XPS spectra of various $InZrO_x$ oxides, in which the abundance of surface oxygen vacancies (O_{defect}, calculated as $I_{defect}/(I_{lattice} + I_{defect})$ are labeled (I_{defect} and $I_{lattice}$ represent peak area of defect and lattice oxygen, respectively)[42]. **b** H_2-TPR profiles of various $InZrO_x$ oxides (The shadow insert is the enlargement of H_2-TPR profiles in the temperature range of 100–250 °C). **c** Cell volumes of various fresh $InZrO_x$ oxides compared to that of H_2-reduced ones. **d** CO_2-TPD profiles of various $InZrO_x$ oxides.

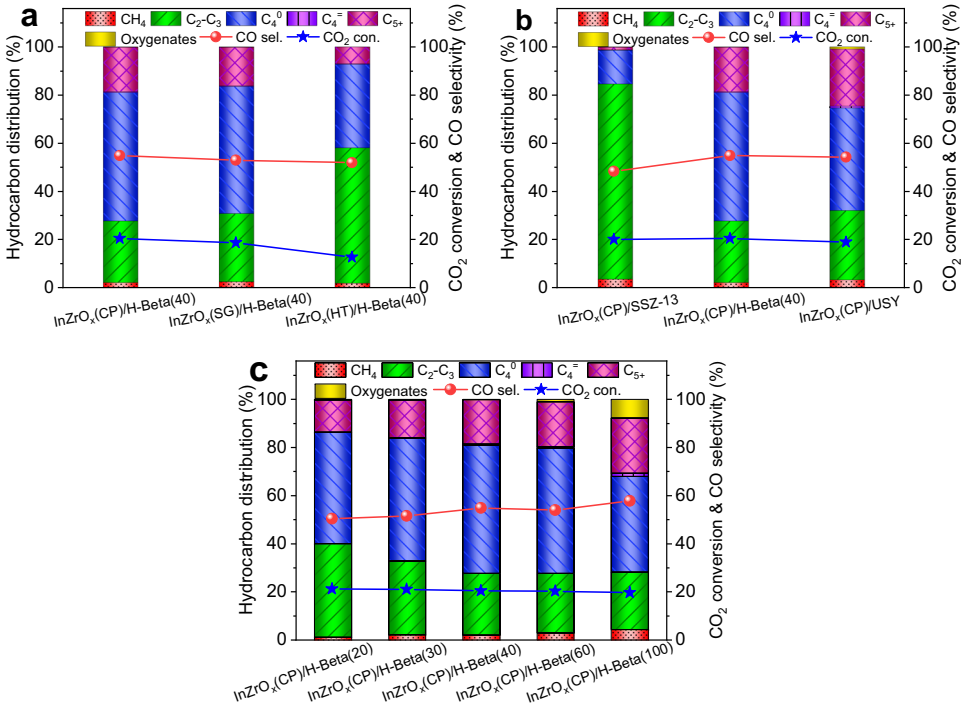

Fig. 3 | Performance of various composite catalysts in the CO_2 hydrogenation. **a**–**c** CO_2 conversion and product distribution for the CO_2 hydrogenation over various $InZrO_x$-Beta(40) composite catalysts (**a**); over $InZrO_x$(CP) composed with different zeolites (**b**); over $InZrO_x$(CP) composed with H-Beta of different Si/Al ratios (**c**). Reaction conditions: 315 °C, 3.0 MPa, SV = 1200 mL g^{-1} h^{-1}, and $H_2/CO_2 = 3$.

hydrogenation to methanol; when composed with H-Beta(40), the $InZrO_x$(CP)-Beta(40) composite catalyst also displays excellent performance in the tandem transformation of CO_2 to butane.

Besides the oxide moiety, the yield and spectrum of hydrocarbon products for the CO_2 hydrogenation are also closely related to the topology framework and acidic properties of the zeotype moiety in the bifunctional composite catalyst. As shown in Fig. 3b, butane appears as the main hydrocarbon product over $InZrO_x$(CP)-Beta, whereas more C_2–C_3 and C_{5+} hydrocarbons are generated over $InZrO_x$(CP)-SSZ-13 and $InZrO_x$(CP)-USY with smaller windows and larger cavities. It

https://doi.org/10.1038/s41467-023-38336-5

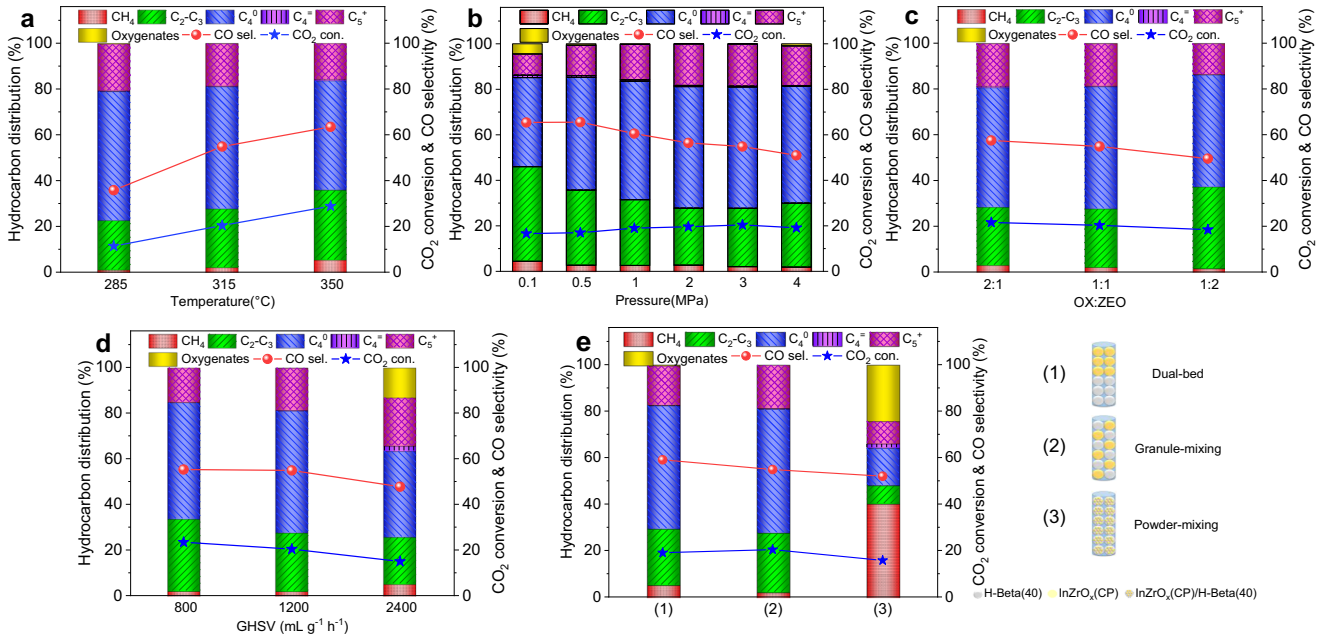

Fig. 4 | Optimization of reaction conditions for the CO_2 hydrogenation. a–e CO_2 conversion and product distribution for CO_2 hydrogenation over the $InZrO_x$(CP)-Beta(40) composite catalyst at different temperatures (**a**), pressures (**b**), oxide/zeolite mass ratios (**c**), space velocities (**d**), and different composing manners of two moieties (**e**). Basic reaction conditions: 315 °C, 3.0 MPa, space velocity of 1200 mL g^{-1} h^{-1}, and H_2/CO_2 ratio of 3 in the feed.

indicates that the 3D 12-ring channels of H-Beta is pertinent for the transformation of methanol-related intermediates (generated from CO_2 hydrogenation over the oxide moiety) into butane.

Moreover, the product distribution for the CO_2 hydrogenation over $InZrO_x$(CP)-Beta is associated with the acid density of the H-Beta zeolite moiety. As shown in Fig. 3c, with an increase of the Si/Al ratio of H-Beta from 20 to 100, the selectivity to C_2–C_3 components decreases, whereas the fraction of C_{5+} components in the product increases, whilst the selectivity to C_4 hydrocarbons (dominated by butane) achieves the maximum value at a Si/Al ratio of 40. A higher Si/Al ratio (viz., less acid sites in H-Beta) may weaken the capability of alkenes hydrogenation and then yield more alkenes. In particular, $InZrO_x$(CP)-Beta(100) displays even an incomplete conversion of methanol due to its rather low acid density. In contrast, excessive acid sites in H-Beta zeolite (e.g. Beta(20), with a very low Si/Al ratio) conduce to the cracking of long-chain hydrocarbons and then generate more small alkenes/alkanes[48]. Therefore, the selectivity to butane shows a volcanic curve with the Si/Al ratio of H-Beta and gets to the maximum value of 53.4% over $InZrO_x$(CP)-Beta(40). Notably, isobutane accounts for 86.5% of two butane isomers.

As water is a co-product in the hydrogenation of CO_2, which acts also vividly in the competitive reverse water-gas (RWGS) reaction[5,6], the possible role of water in the reaction process was further evaluated by adding different proportions of water into the H_2 and CO_2 feed. As shown in Supplementary Fig. 11a, when water is introduced into the reaction system after about 16 h, the CO_2 conversion decreases from 19.1 to 8.9%, along with the attenuation of the selectivity to CO from 54.7 to 34.0%. Such a phenomenon becomes more evident when the proportion of water in the feed increases from 7.5 to 15.1% (Supplementary Fig. 11b), where the CO_2 conversion and selectivity to CO decreases considerably to 7.3% and 26.1%, respectively. This can be explained by the fact that more water in the reaction mixture can effectively counteract the RWGS reaction ($CO_2 + H_2 = CO + H_2O$), leading to the decline of the CO_2 conversion and the selectivity to CO[5,6,9]. In addition, water molecules may also compete for the active adsorption sites with the reactants, which may also abate the conversion of CO_2 to hydrocarbons.

It is noteworthy that the conversion of CO_2 and selectivity to CO are both spontaneously rejuvenated, when the co-feeding water is cut off (Supplementary Fig. 11c). However, the CO_2 conversion cannot be fully recovered to the original value, implying that co-feeding water has certain impact on the catalytic activity of the $InZrO_x$ oxide. The XRD patterns and TEM images of the spent catalysts shown in Supplementary Fig. 12 indicate that after the CO_2 hydrogenation with co-feeding water, the particle size of $InZrO_x$ oxide increases considerably, along with the decrease of surface area and pore volume (Supplementary Fig. 13a and Supplementary Table 3). This leads to a decrease in the surface oxygen vacancies concentration, which can weaken the CO_2 adsorption capacity, as indicated by the O 1*s* XPS and CO_2-TPD results (Supplementary Fig. 13b, c), although the In, Zr and O elements are still uniformly dispersed with each other in the $InZrO_x$ oxide (Supplementary Fig. 14). Nevertheless, the selectivity to butane changes very little during the reaction. This is ascribed to the fact that the crystal structure, morphology, and particle size of H-Beta zeolite, which determine the manner for the formation of hydrocarbons from the methanol-related intermediates, are well maintained during the CO_2 hydrogenation with co-feeding different contents of water (Supplementary Fig. 15).

Optimization of reaction conditions

The reaction temperature has a great influence on the product yield and spectrum for the hydrogenation of CO_2 over $InZrO_x$(CP)-Beta(40). As shown in Fig. 4a, with the increase of temperature from 285 to 350 °C, as expected, the CO_2 conversion increases from 11.4% to 28.8%, despite that more CO are produced due to the promotion of the reverse water-gas shift (RWGS) reaction at a higher temperature[5,6]. Meanwhile, the selectivity to butane and C_{5+} decreases gradually with the increase of temperature, accompanied by the formation of more C_1–C_3 products due to the aggravated cracking of long-chain hydrocarbons, as also observed by Ding and co-workers[49].

In contrast, an increase of the reaction pressure from 0.1 to 3.0 MPa (at 315 °C) elevates the CO_2 conversion from 16.6 to 20.4%, but decreases the selectivity to CO from 65.4 to 54.9%, as shown in Fig. 4b. Meanwhile, the selectivity to butane is raised from 39.1 to 53.4%,

https://doi.org/10.1038/s41467-023-38336-5

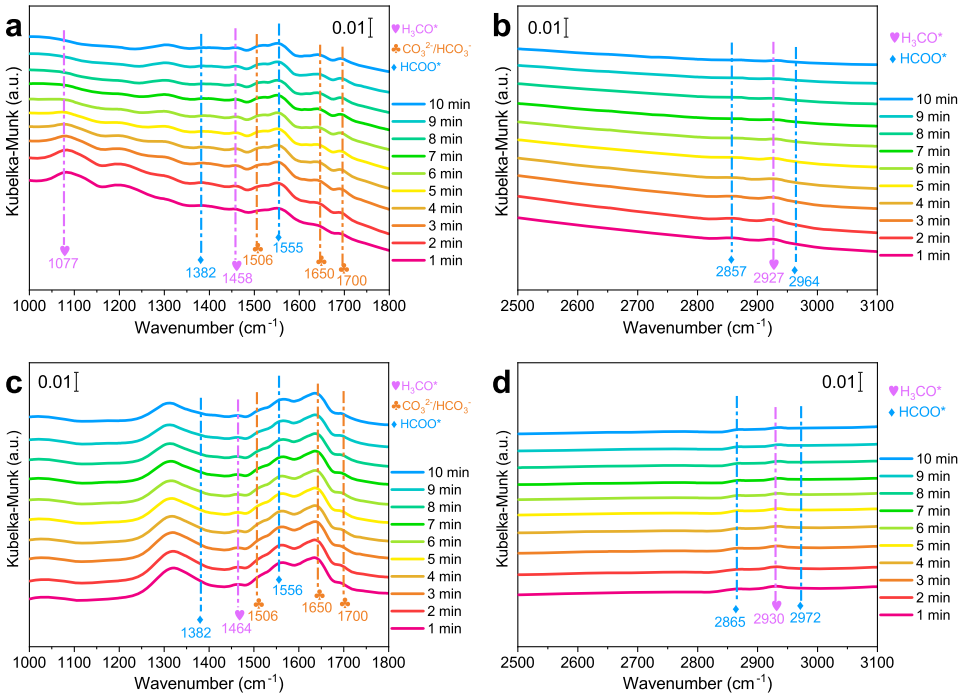

Fig. 5 | In situ DRIFT spectra. a–d In situ DRIFT spectra of $InZrO_x$(CP) (**a**, **b**) and $InZrO_x$(HT) (**c**, **d**) in CO_2 hydrogenation. The spectra were collected every 1 min up to 10 min after pretreating the sample under Ar atmosphere (30 mL min^{-1}) for 0.5 h at 200 °C and 0.1 MPa and purging with the H_2 and CO_2 mixture (40 mL min^{-1}, $H_2/CO_2 = 3$).

accompanied by a gradual decline of the selectivity to alkenes, as a higher hydrogen pressure conduces to the hydrogenation of alkenes. However, a further increase of pressure to 4.0 MPa leads to the formation of more C_1–C_3 alkanes, at the expense of butane and C_{5+} hydrocarbons.

The effect of the oxide/zeolite mass ratio in the $InZrO_x$(CP)-Beta(40) composite on the CO_2 hydrogenation was also considered, as demonstrated in Fig. 4c. With a decrease of the oxide/zeolite mass ratio from 2 to 1/2, the CO_2 conversion and selectivity to CO decrease from 21.7% and 57.5% to 18.5% and 49.6%, respectively, while the highest selectivity to butane (53.4%) is achieved at an oxide/zeolite mass ratio of 1.

The space velocity and H_2/CO_2 ratio in the feed also have certain influence on the CO_2 hydrogenation. A decrease of the space velocity from 2400 to 800 mL g^{-1} h^{-1} makes the CO_2 conversion increase from 14.9 to 23.4%, despite that the formation of CO is also promoted (Fig. 4d), whilst the selectivity to butane gets the maximum value of 53.4% at a space velocity of 1200 mL g^{-1} h^{-1}. In addition, elevating the H_2/CO_2 ratio from 3 to 6 in the feed raises the CO_2 conversion from 20.4 to 25.6% and decreases the selectivity to CO slightly from 54.9 to 51.2%, while it has little influence on the selectivity to butane, as shown in Supplementary Fig. 16.

In addition, the manner used to compose the $InZrO_x$-Beta bifunctional catalysts also displays a significant influence on the CO_2 hydrogenation. As shown in Fig. 4e, a decrease in the contact distance between $InZrO_x$(CP) and H-Beta(40) from dual-bed filling to granule stacking makes the CO_2 conversion and selectivity to butane slightly increase from 19.1% and 53.1% to 20.4% and 53.4%, respectively. However, the composite catalyst prepared by powder mixing of the two moieties just produces large amounts of methane (40.2%) and methanol (24.2%), due to the rapid deactivation of H-Beta zeolite. Similar phenomenon was also observed by Wang and co-workers[45]; that is, the In species may easily migrate from the metal oxide moiety to the zeotype moiety when the two moieties are in very close contact, resulting in the rapid passivation of the acid sites in the zeotype moiety that are responsible for the successive transformation of methanol-related intermediates to hydrocarbons.

On all accounts, the bifunctional $InZrO_x$(CP)-Beta(40) composite catalyst composed by granule stacking with equal mass of oxide and zeolite exhibits excellent performance in the selective hydrogenation of CO_2 to butane. Under 315 °C, 3.0 MPa, a space velocity of 1200 mL g^{-1} h^{-1}, and an H_2/CO_2 ratio of 3 in the feed, a high selectivity of 53.4% to butane in all hydrocarbons is achieved, at a CO_2 conversion of 20.4% and a selectivity of only about 2% to CH_4.

Reaction mechanism of the CO_2 hydrogenation to butane

To reveal the reaction mechanism, in situ DRIFTs were first performed for the CO_2 hydrogenation to methanol over the $InZrO_x$(CP), $InZrO_x$(SG), and $InZrO_x$(HT) oxides, as shown in Fig. 5a–d and Supplementary Fig. 17. After introducing H_2 and CO_2 for reaction over $InZrO_x$(CP) for 1 min, the vibration bands attributed to the carbonate (CO_3^{2-}/HCO_3^-) species appear at 1506, 1650, and 1700 cm^{-1} [50–52], belonging to the signals of activated CO_2 (Fig. 5a, b). Besides, the characteristic peaks assigned to the formate (HCOO*) species at 1382, 1555, 2857, and 2964 cm^{-1} are quickly observed[15,53]. Meanwhile, the peaks at around 1077, 1458, and 2927 cm^{-1} ascribed to the methoxy (H_3CO*) species are simultaneously detected[15,53,54]. With the proceeding of the reaction process, the peak intensity of HCOO* and H_3CO* species decreases gradually, as they are hydrogenated to methanol. Such phenomena confirm that formate and methoxy are crucial intermediates for methanol formation in the CO_2 hydrogenation over $InZrO_x$(CP), in line with the previous reports[15,53]. In comparison with $InZrO_x$(CP), $InZrO_x$(SG) and $InZrO_x$(HT) also show the characteristic peaks of the formate and methoxy species, but in a much lower intensity (Fig. 5c, d and Supplementary Fig. 17), corresponding to their less oxygen vacancies and poorer catalytic performance in the CO_2 hydrogenation.

The methanol-related intermediates generated on the $InZrO_x$ oxide are further transformed into hydrocarbons on the acid sites of the H-Beta zeolite, which can be consolidated by the control

https://doi.org/10.1038/s41467-023-38336-5

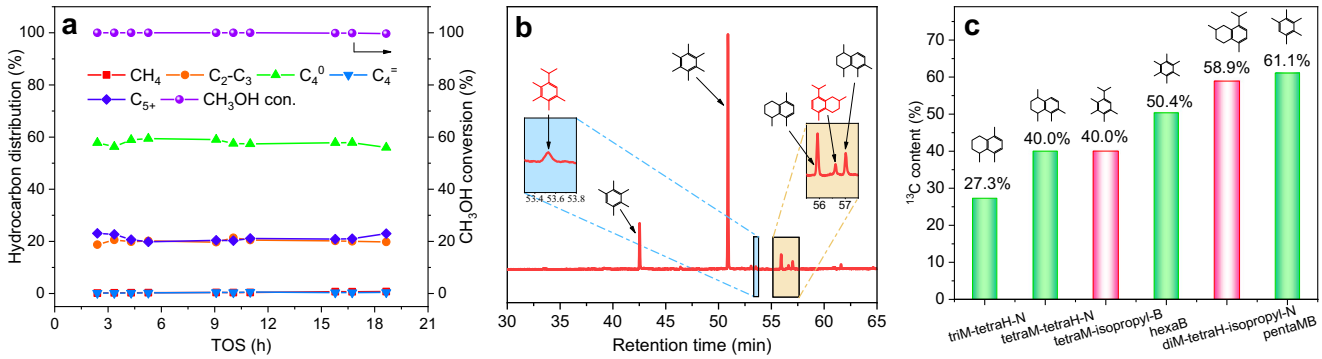

Fig. 6 | Probe experiments for methanol conversion. a Methanol conversion and product distribution for MTH in H_2 atmosphere over H-Beta(40) zeolite with a methanol WHSV of 0.05 h^{-1}. **b** GC-MS chromatograms of residual species in H-Beta(40) after the MTH reaction in H_2 atmosphere with a methanol WHSV of 0.05 h^{-1} (The shadow inserts are the enlargement of GC-MS chromatograms at specified retention times). **c** ^{13}C content of the confined organic species in H-Beta(40), obtained from $^{12}C/^{13}C$ methanol switching experiment.

experiments for methanol conversion (viz., methanol to hydrocarbons, MTH) in the H_2 atmosphere over the H-Beta(40) zeolite. As shown in Fig. 6a, butane is the dominant product in MTH; in addition, the selectivity to butane (58.0%) here in MTH over H-Beta(40) is highly comparable to that in the CO_2 hydrogenation over $InZrO_x$-Beta(40) (53.4%).

After the MTH reaction, the residual species in the H-Beta zeolite were extracted and detected by GC-MS[55]. As demonstrated in Fig. 6b, higher polymethylbenzens (polyMBs, e.g., pentaMB and hexaMB) are found to be the dominant hydrocarbon pool (HCP) species generated in the methanol conversion process over the H-Beta zeolite, which could quickly grow up into aromatics containing isopropyl side-chain via continuous methylation reactions. It is known that these polyMBs are responsible for the propene formation via the side-chain aromatic-based cycle[56,57]. After the elimination of isopropyl side-chain, the generated propene can be further converted to butane through methylation and subsequent hydrogenation reactions. In fact, certain polyMBs and polymethylnaphthalenes (polyMNs) with isopropyl side-chain (e.g. 1-isopropyl-2,3,4,5-tetramethylbenzene (isopropyl-MB) and 8-isopropyl-2,5-dimethyl-1,2,3,4-tetrahydronaphthalene (isopropyl-MN)) are simultaneously detected by GC-MS (Fig. 6b). Meanwhile, in the $^{12}C/^{13}C$-methanol isotope switching experiments, these higher polyMBs and even polyMNs were labeled by a high content of ^{13}C (e.g. 61.1% of hexaMB and 58.9% of isopropyl-MN), according well with their high activity in MTH (Fig. 6c).

Furthermore, as expected, these polyMBs and polyMNs as the HCP species are also detected on the spent $InZrO_x$(CP)-Beta(40) catalyst after the CO_2 hydrogenation test, as shown in Supplementary Fig. 18. In contrast, the content of polyMBs and polyMNs containing isopropyl side-chain on the spent $InZrO_x$(HT)-Beta(40) catalyst is rather lower than that on the spent $InZrO_x$(CP)-Beta(40) catalyst (Supplementary Fig. 19), corresponding to the rather lower activity of $InZrO_x$(HT) in the CO_2 hydrogenation to methanol; that is, as less methanol-related intermediates are formed on the $InZrO_x$(HT) moiety with poorer activity in the CO_2 hydrogenation, the formation and growth of higher polyMBs as the HCP species for MTH are also greatly restricted in the H-Beta moiety, leading to the lower yield of butane over the $InZrO_x$(HT)-Beta composite catalyst (Fig. 3a).

The reaction kinetics for butane formation was further investigated by DFT calculation. As shown in Fig. 7 and Supplementary Fig. 20, isopropyl-MB and isopropyl-MN are first protonated to the corresponding carbocations, with a free energy barrier of 79 and 69 kJ mol^{-1}, respectively. The elimination of isopropyl group from these two carbocations to form the propoxy species on the acid sites requires a low free energy barrier of 69 and 47 kJ mol^{-1}, with a high rate constant of 8.76×10^6 and 8.45×10^8 s^{-1}, respectively, similar to those reported previously[56]. Propene is then obtained from the deprotonation of propoxy with a free energy barrier of 70 kJ mol^{-1} and a rate constant of 8.20×10^6 s^{-1}. Further conversion of propene to butoxy and then to iso-butane via methylation, isomerization, and hydrogenation reactions needs to overcome a free energy barrier of 124, 48, and 47 kJ mol^{-1}, respectively.

In addition, as given by the calculated free energy surface, the overall free energy height for the butane formation over H-Beta is only 115 kJ mol^{-1}, with an overall reaction free energy of −104 kJ mol^{-1}. All these evince that butane can be generated easily from the methanol-related intermediates via the side-chain route of aromatic-based cycle in the H-Beta zeolite.

On all accounts, the CO_2 hydrogenation over a bifunctional catalyst relies on both the oxide and the zeotype moieties. For the $InZrO_x$-Beta composite, the $InZrO_x$ moiety is responsible for the conversion of CO_2 to the methanol-related intermediates (similar to methanol synthesis), whereas the H-Beta moiety is accountable to the subsequent transformation of methanol-related intermediates into hydrocarbons (similar to methanol to hydrocarbons (MTH), via the hydrocarbon pool mechanism). As a result, the conversion of CO_2 is mainly related to the $InZrO_x$ moiety; $InZrO_x$(CP) prepared by co-precipitation has abundant oxygen vacancies and great capacity for the CO_2 hydrogenation to methanol. In contrast, the product distribution is mainly associated with the framework topology and acidity properties of the zeotype moiety. The H-Beta zeolite of 3D 12-ring channels with moderate acidity (Si/Al = 40) is appropriate for the construction of HCP containing abundant higher polyMBs and polyMNs as well as the production of butane via the aromatic-based cycle of HCP mechanism through the isopropyl side-chain elimination and subsequent methylation and hydrogenation reactions. In addition, the granule-mixing manner used to compose the $InZrO_x$-Beta bifunctional catalyst can realize a pertinent contact between two moieties and then achieve a prominent coupling of two reaction steps (viz., CO_2 hydrogenation to methanol and MTH).

Surface silica modification to restrict the in migration

The degeneration of either the metal oxide moiety or the zeotype moiety can deactivate the whole bifunctional OX-ZEO catalyst system in the hydrogenation of CO_2 to hydrocarbons[58,59]. The degeneration of metal oxide often causes a rapid decrease in the CO_2 conversion, as the adsorption and activation of CO_2 are mainly performed on the surface of metal oxide[37,43]. As for the acidic zeolite, it catalyzes the subsequent transformation of the methanol-related intermediates previously generated on the oxide moiety into hydrocarbons; the rapid increase in the selectivity to unconverted methanol is an important sign for the deactivation of the zeolite component[45,60,61]. For the In-based

https://doi.org/10.1038/s41467-023-38336-5

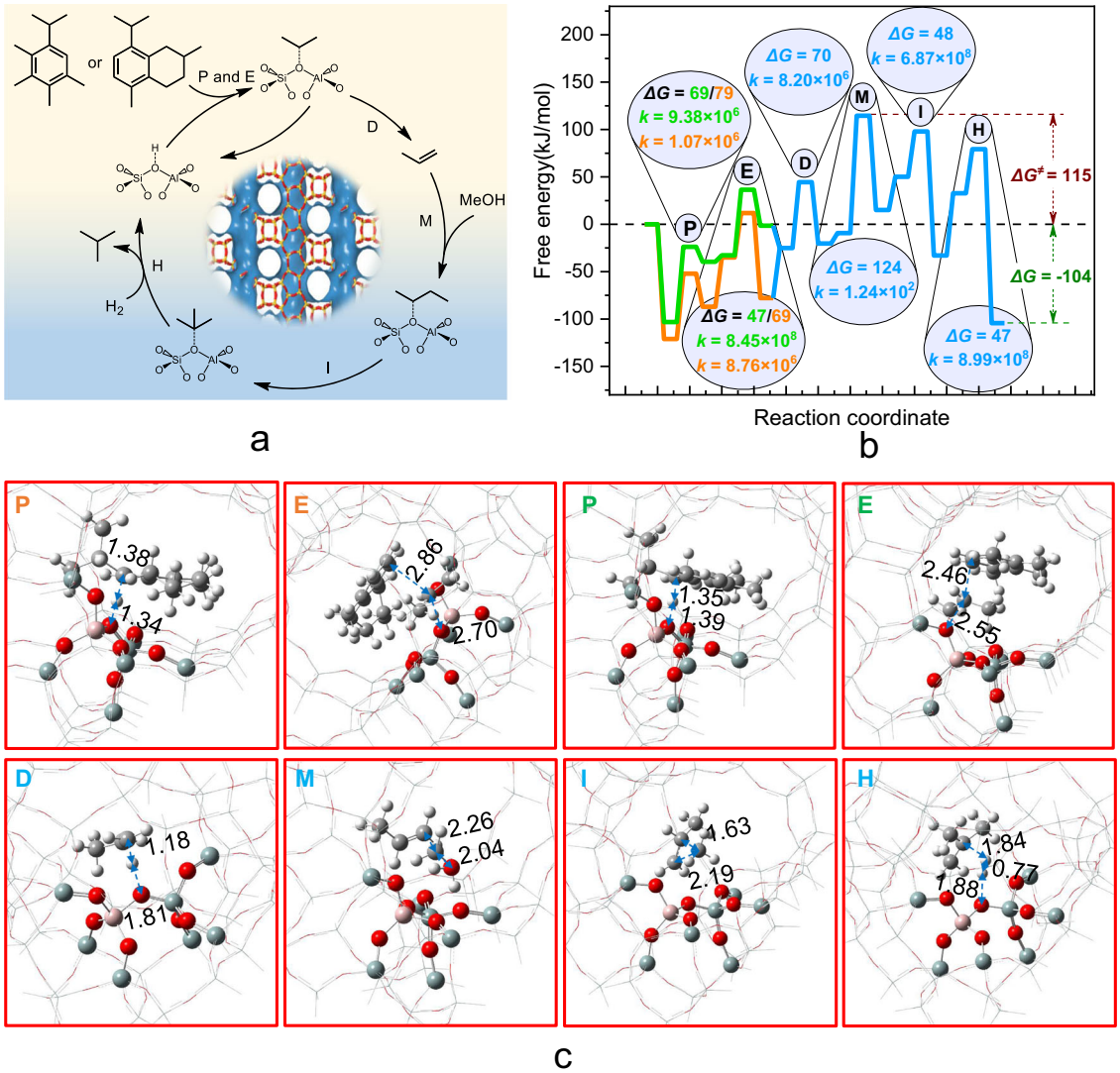

Fig. 7 | DFT calculations. a Reaction scheme of butane formation via the side-chain route of aromatic-based cycle. **b** Free energy profiles for butane formation from 8-isopropyl-2,5-dimethyl-1,2,3,4-tetrahydronaphthalene (orange/blue line) or 1-isopropyl-2,3,4,5-tetramethylbenzene (green/blue line) at 315 °C over H-Beta zeolite, where the overall free energy height ($\Delta G^{\neq}$) and overall reaction free energy (ΔG) in kJ mol^{-1} are labeled. **c** Optimized transition states of various reaction steps, including protonation (P), elimination (E), deprotonation (D), methylation (M), isomerization (I), and hydrogenation (H); atom coloring: cyan (Si), red (O), white (H), pink (Al).

bifunctional catalyst, the indium species may facilely migrate from the oxide moiety into the zeotype moiety in the H_2-containing atmosphere, which can passivate the acid sites in the zeotype moiety and then rapidly deactivate the whole composite catalyst used in the CO_2 hydrogenation by lowering capacity of the acidic zeolite component in the transformation of methanol-related intermediates to hydrocarbons[45].

As shown in Fig. 8a, methanol and dimethyl ether (DME) are clearly detected for the CO_2 hydrogenation over $InZrO_x$(CP)-Beta(40) after reaction for 42 h on stream; thereafter, the selectivity to methanol and DME increases quickly, accompanied by a considerable decrease of the selectivity to butane, suggesting the rapid degeneration of the Beta zeolite. Meanwhile, more CO is generated, due to the shrinking of the methanol conversion capacity of the H-Beta zeolite that may relatively promote the competitive RWGS reaction[5]. After the reaction test, certain amounts of the In element are detected in the H-Beta moiety (Supplementary Table 4), indicating the serious phase segregation of $InZrO_x$(CP) during the CO_2 hydrogenation reaction. In fact, the migration of indium species turns to be a fatal defect for the application of the In-based bifunctional catalyst in practice for the hydrogenation of CO_2 to hydrocarbons; it is pressing but also rather challenging to effectively inhibit the migration of the In species.

To improve the structural stability of the In-based catalyst in the CO_2 hydrogenation, a surface silica protection strategy was adopted in current work; that is, certain amount of SiO_2 (4 wt.% for $InZrO_x$(SCP-4) and 8 wt.% for $InZrO_x$(SCP-8)) was deposited on the $InZrO_x$(CP) oxide through impregnation with tetraethylorthosilicate (TEOS) solution and subsequent calcination at 500 °C (Supplementary Fig 21a). The XRD patterns shown in Fig. 9a indicate that the surface silica modification has little impact on the crystal structure of $InZrO_x$(CP). In addition, no diffraction peaks of SiO_2 are detected, suggesting that SiO_2 is highly dispersed on the $InZrO_x$ surface and/or present in amorphous phase. The EDX elemental mapping results show that the silica species are evenly distributed on the surface of $InZrO_x$(CP), despite that they cannot be clearly distinguished by XRD, HR-TEM and Aberration-corrected HAADF-STEM (Fig. 9a and Supplementary Figs. 22–24), which consolidates the high dispersion of silica in the SiO_2-modified $InZrO_x$ oxide. The SiO_2-modified $InZrO_x$(SCP-4) and $InZrO_x$(SCP-8) oxides also show larger surface area than $InZrO_x$(CP), as revealed by the N_2 sorption results (Supplementary Fig. 25 and

https://doi.org/10.1038/s41467-023-38336-5

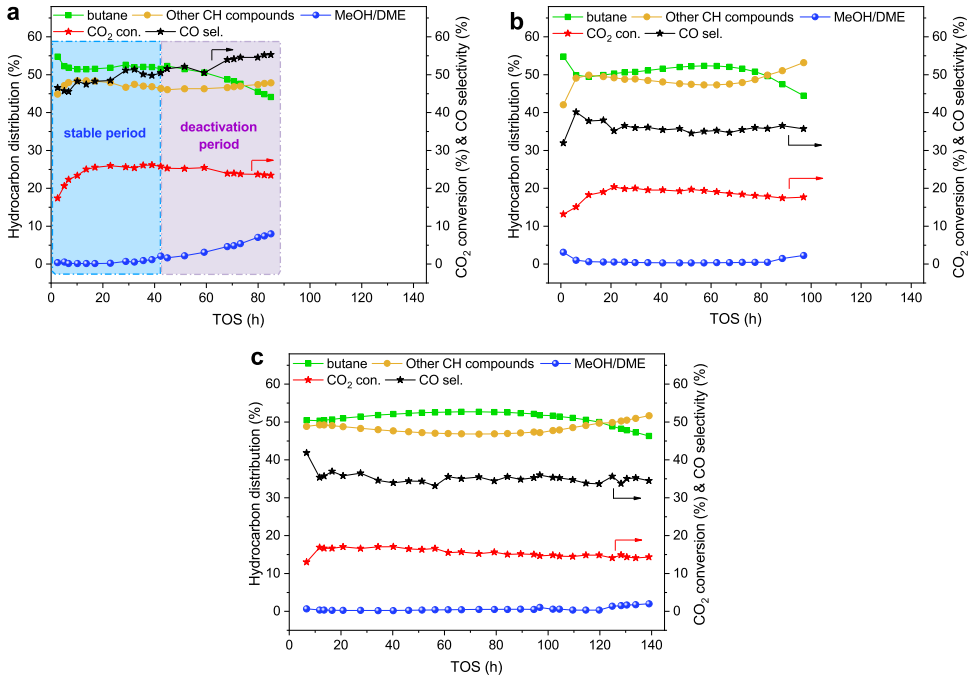

Fig. 8 | Catalytic stability of SiO_2-modified $InZrO_x$-Beta catalyst. a–c CO_2 conversion and product distribution for CO_2 hydrogenation to butane over $InZrO_x$(CP)-Beta(40) (**a**), $InZrO_x$(SCP-4)-Beta(40) (**b**), and $InZrO_x$(SCP-8)-Beta(40) (**c**). Reaction conditions: 315 °C, 3.0 MPa, 1200 mL g^{-1} h^{-1} and H_2/CO_2 = 6. The catalyst lifetime is defined as the time on stream when the selectivity to methanol and DME reaches 2% for CO_2 hydrogenation over the bifunctional catalyst.

Supplementary Table 5). Besides, the SiO_2-modified $InZrO_x$(SCP-4) and $InZrO_x$(SCP-8) oxides have the average particle size of 6.10 and 4.70 nm, respectively, much smaller than that of the unmodified $InZrO_x$ (9.76 nm) (Supplementary Fig. 26), suggesting that the silica modification can also inhibit the agglomeration of $InZrO_x$ upon calcination at high temperature.

Moreover, the XPS spectra shown in Fig. 9b–d illustrate that the In 3*d* and Zr 3*d* signals of silica-modified $InZrO_x$(SCP-4) and $InZrO_x$(SCP-8) shift towards higher binding energies, whereas the Si 2*p* signal moves to lower value, compared to the corresponding signals of the unmodified $InZrO_x$(CP) counterpart. This is indicative of a strong interaction between the $InZrO_x$(CP) and silica species, which is confirmed by the H_2-TPR results; the reduction of both defect In_2O_3 sites and bulk In_2O_3 in $InZrO_x$(SCP-4) and $InZrO_x$(SCP-8) requires higher temperature than that in the unmodified $InZrO_x$(CP) counterpart (Fig. 9e). The strong interaction between the $InZrO_x$ and silica species is further corroborated by the calculated projected density of states (PDOS) and charge difference density (CDD) results. As shown in Supplementary Fig. 27, strong electron donation and back-donation are observed between the surface silica species and $InZrO_x$ oxide in the CDD plot, substantiating an intense interaction of the Si 2*p* orbitals with the In 3*d* orbitals around Fermi level. Such strong interaction makes the reduction and migration of indium species in the silica-modified $InZrO_x$(SCP-4) and $InZrO_x$(SCP-8) oxides more difficult than that in the unmodified $InZrO_x$(CP) counterpart.

A schematic diagram is then plotted in Supplementary Fig. 21b to illustrate the mechanism of enhancing structural and catalytic stability of the $InZrO_x$-Beta composite by the surface silica protection strategy. For the un-protected $InZrO_x$ oxide, indium species may be easily reduced to metallic In species in the reductive atmosphere, which facilely migrate to the H-Beta component and then passivate the acid sites, leading to the rapid deactivation of the composite catalyst. In contrast, after the surface silica modification, the strong interaction between the SiO_2 and $InZrO_x$ species can suppress the reduction of In_2O_3 to metallic indium species and then effectively hinder the metallic indium species from migration into the H-Beta component. Consequently, the structural and catalytic stability of the $InZrO_x$-Beta composite during the reduction and CO_2 hydrogenation processes can be greatly improved by the surface silica protection strategy.

The catalytic performance of $InZrO_x$(SCP-4)-Beta(40) and $InZrO_x$(SCP-8)-Beta(40) in the CO_2 hydrogenation was then compared with that of the $InZrO_x$(CP)-Beta(40) counterpart. As shown in Fig. 8b and Supplementary Fig. 28a, the reaction time when the selectivity to unconverted methanol reaches 2% is considerably prolonged from about 42 h of $InZrO_x$(CP)-Beta(40) to 97 h of $InZrO_x$(SCP-4)-Beta(40) under the same conditions, indicating the higher catalytic stability of latter $InZrO_x$(SCP-4)-Beta(40). Meanwhile, the acidic properties of the H-Beta zeolite component separated from various spent $InZrO_x$-Beta composite catalysts after reaction for the same time were evaluated, as demonstrated in Supplementary Fig. 29 and Supplementary Table 6. Apparently, after reaction for 24 and 42 h, the total acid content and strong acid content of H-Beta zeolite separated from the spent $InZrO_x$(SCP-4)-Beta(40) catalyst are both much higher than that separated from the $InZrO_x$(CP)-Beta(40) counterpart. This further confirms that the surface silica protection strategy to alleviate the rapid passivation of the acid sites in H-Beta is rather effective in improving the stability of the bifunctional $InZrO_x$-Beta composite catalyst in the CO_2 hydrogenation to hydrocarbons.

In addition, the selectivity to CO over $InZrO_x$(SCP-4)-Beta(40) is reduced to 34.5% from the value of 51.2% over $InZrO_x$(CP)-Beta(40), being much lower than those reported for the In-based bifunctional catalysts in the CO_2 hydrogenation in the literature at a similar CO_2 conversion (Supplementary Table 7). Through a further increase of the SiO_2 loading to 8 wt.%, the catalytic lifetime (e.g. the reaction time when the selectivity to unconverted methanol reaches 2%) of $InZrO_x$(SCP-8)-Beta(40) is further prolonged to above 140 h, along with a lower selectivity to CO (33.1%), as shown in Fig. 8c.

Notably, although the selectivity to butane keeps at around 53% over both the SiO_2-modified and unmodified $InZrO_x$-Beta catalysts during the steady stage, the selectivity to butane for the CO_2 hydrogenation over the $InZrO_x$(SCP-4)-Beta(40) and $InZrO_x$(SCP-8)-Beta(40) composite catalysts still decreases gradually after a long time on

https://doi.org/10.1038/s41467-023-38336-5

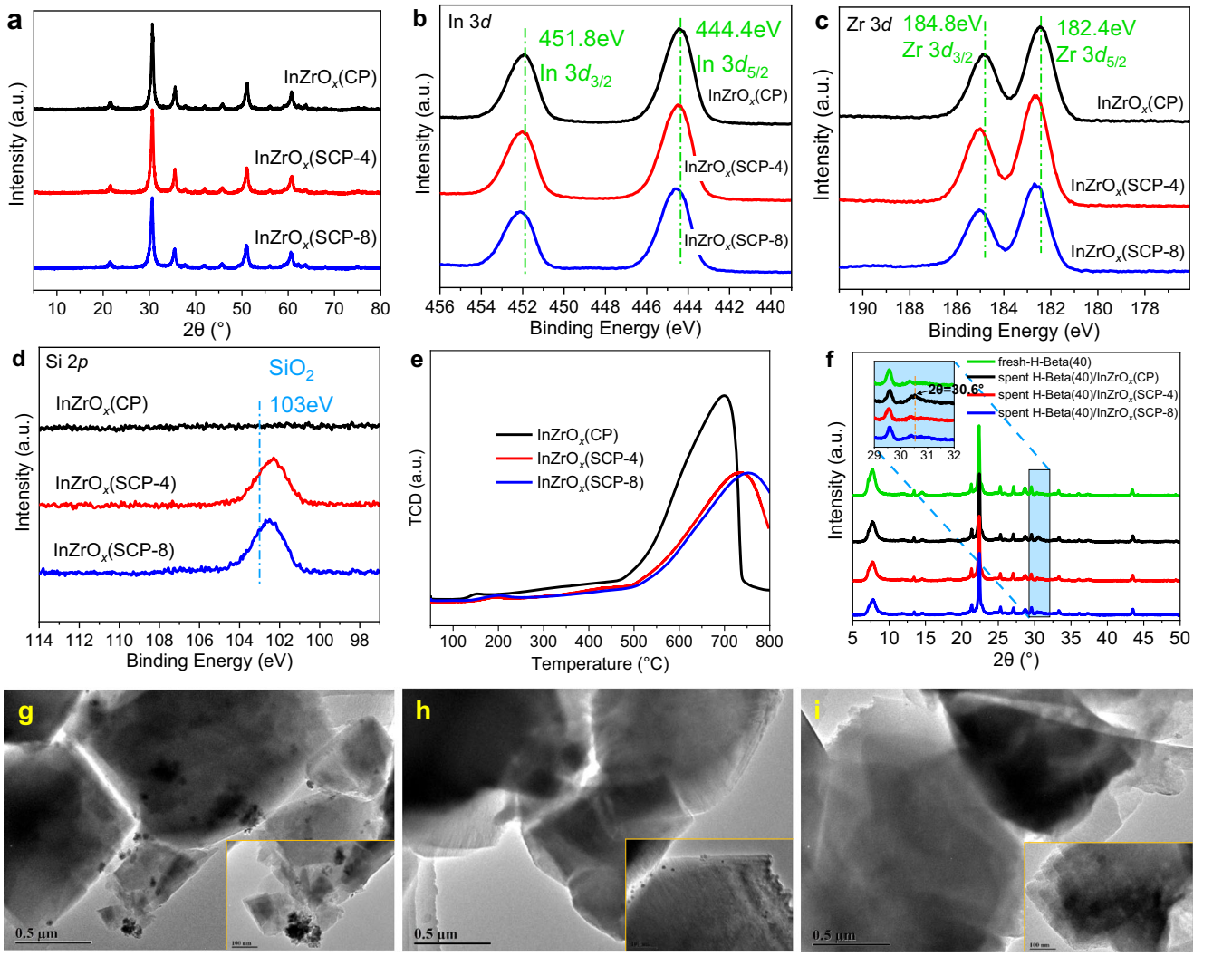

Fig. 9 | Structure and electronic state of SiO_2-modified $InZrO_x$-Beta. a XRD patterns of fresh $InZrO_x$(CP), $InZrO_x$(SCP-4) and $InZrO_x$(SCP-8). **b**–**d** In 3*d* (**b**), Zr 3*d* (**c**) and Si 2*p* (**d**) XPS spectra of fresh $InZrO_x$(CP), $InZrO_x$(SCP-4) and $InZrO_x$(SCP-8). **e** H_2-TPR profiles of fresh $InZrO_x$(CP), $InZrO_x$(SCP-4) and $InZrO_x$(SCP-8). **f** XRD patterns of H-Beta(40) zeolite separated from the spent $InZrO_x$(CP)-Beta(40), $InZrO_x$(SCP-4)-Beta(40) and $InZrO_x$(SCP-8)-Beta(40) composite catalysts (The shadow insert is the enlargement of XRD patterns in the 2θ range of 29–32°). **g**–**i** TEM images of the spent H-Beta(40) zeolite separated from $InZrO_x$(CP)-Beta(40) (**g**), $InZrO_x$(SCP-4)-Beta(40) (**h**) and $InZrO_x$(SCP-8)-Beta(40) (**i**) composite catalysts.

stream (ca. 70–100 h). It indicates that the surface silica modification method may not completely and eternally solve the problem of indium species migration. Nevertheless, the onset time for the decrease in the selectivity to butane is extended from 40 h of $InZrO_x$(CP)-Beta(40) to ca. 70 h of $InZrO_x$(SCP-4)-Beta(40) and ca. 100 h of $InZrO_x$(SCP-8)-Beta(40), as demonstrated in Supplementary Fig. 28b. This also suggests that an increase of the SiO_2 loading is favorable for lowering the impact of indium migration on the butane formation. However, the deposited SiO_2 may also cover a fraction of the surface oxygen vacancies, which leads to a decrease of CO_2 adsorption capacity on the SiO_2-modified $InZrO_x$ oxides (Supplementary Fig. 30). As shown by the O 1*s* XPS spectra in Supplementary Fig. 31, $InZrO_x$(SCP-4) and $InZrO_x$(SCP-8) have a lower concentration of surface oxygen vacancies but abundant OH groups originated from the surface Si–OH of SiO_2, in comparison with the $InZrO_x$(CP) counterpart. Consequently, the CO_2 conversion is also decreased from 25.6% over $InZrO_x$(CP)-Beta(40) to 19.7% over $InZrO_x$(SCP-4)-Beta(40), and further to 16.6% over $InZrO_x$(SCP-8)-Beta(40). Accordingly, the loading of SiO_2 for the surface protection of the $InZrO_x$ oxide should be restricted to a certain value (ca. 4–8 wt.%) to elevate the catalytic stability of catalyst and meanwhile avoid a substantial decrease of the CO_2 conversion.

After the reaction test, the granules of $InZrO_x$(CP) oxide and H-Beta zeolite in the $InZrO_x$(CP)-Beta composite were separated from each other and then characterized by various measures. According to the TG analysis results (Supplementary Fig. 32), all three samples show a very low coking rate (ca. 0.0003–0.0005 h^{-1}), indicating that the coke deposition here should not be the major cause of catalyst deactivation. Unlike the conversion of methanol to hydrocarbons (MTH) over a zeolite catalyst in the N_2 or Ar atmosphere, for the hydrogenation of CO_2 to hydrocarbons, the presence of H_2 and H_2O in high pressure can effectively eliminate the coke precursors and thus greatly hinder the formation and accumulation of coke species. However, in the XRD patterns shown in Fig. 9f, one obvious diffraction peak at ca. 30.6° ascribed to the (222) crystal facet of In_2O_3 is distinctly detected on the H-Beta zeolite separated from the spent $InZrO_x$(CP)-Beta(40) catalyst, which is further verified by the identification of $InZrO_x$ nano-particles in the TEM image on the surface of separated H-Beta zeolite (Fig. 9g). In contrast, such In species are nearly undetectable on the H-Beta zeolite separated from the spent $InZrO_x$(SCP-4)-Beta and $InZrO_x$(SCP-8)-Beta catalysts (Fig. 9h/i), suggesting that the phase segregation of $InZrO_x$ and the migration of indium species are effectively slowed down on the SiO_2-modified

$InZrO_x$(SCP-4) and $InZrO_x$(SCP-8) oxides during the CO_2 hydrogenation reaction.

In addition, after reaction for 100 h over $InZrO_x$(SCP-4) and 140 h over $InZrO_x$(SCP-8), the diffraction peaks in the XRD patterns and the binding energies in the In 3*d*, Zr 3*d* and Si 2*p* XPS spectra of the spent $InZrO_x$(SCP-4) and $InZrO_x$(SCP-8) oxides are highly comparable to those of the corresponding fresh ones (Supplementary Fig. 33). Meanwhile, the lattice spacing of 0.290–0.291 nm, assigned to the (222) crystal facet of In_2O_3, is clearly visible on the Aberration-corrected HAADF-STEM images and HR-TEM images of the spent $InZrO_x$(SCP-4) and $InZrO_x$(SCP-8) oxides (Supplementary Fig. 34), along with the uniform distribution of In, Zr, O and Si elements over these two samples (Supplementary Figs. 35, 36). The TEM images suggests that the spent $InZrO_x$(SCP-4) and $InZrO_x$(SCP-8) samples have a particle size of 7.57 and 5.16 nm, respectively, only slightly larger than the values of 6.10 and 4.70 nm for the fresh $InZrO_x$(SCP-4) and $InZrO_x$(SCP-8) counterparts, respectively (Supplementary Fig. 37). All these results reveal that the surface silica protection strategy used in current work is rather effective in suppressing the phase segregation of $InZrO_x$ oxide moiety and avoiding the rapid poisoning of the acid sites in the zeolite moiety induced by the In migration, which can thus significantly improve the structural and catalytic stability of the In-based oxide-zeolite composite catalyst in the CO_2 hydrogenation.

As expected, such a strategy can also be extended to the SiO_2-modified In_2O_3-Beta catalyst. As shown in Supplementary Fig. 38a, the In_2O_3(SCP-4)-Beta(40) catalyst shows a long catalytic lifetime (ca. 65 h) and high selectivity to butane (ca. 53% in hydrocarbons) in the CO_2 hydrogenation. In contrast, over the unmodified In_2O_3(CP)-Beta(40) counterpart, the selectivity to butane is quickly decreased to 30%, along with the generation of much more unconverted methanol (25%) after reaction for ca. 65 h (Supplementary Fig. 38b). Undoubtedly, the improved stability of the In_2O_3(SCP-4)-Beta(40) catalyst also originates from the inhibition of the indium species from reduction and migration by the surface silica protection, which can alleviate the rapid deactivation of the zeolite moiety in the hydrogenation of CO_2 to hydrocarbons (Supplementary Fig. 38c–e).

It is noteworthy that although the strong interaction between the surface SiO_2 species and $InZrO_x$ oxide can inhibit the indium species from easy reduction and migration and then improve the stability of the $InZrO_x$-Beta composite catalyst in the CO_2 hydrogenation, it does not relocate the indium species on the composite catalyst. In other words, the silica species are only highly dispersed on the surface of $InZrO_x$ oxide and do not cause any significant structural distortion and/or rearrangement of the $InZrO_x$ oxide upon the reduction and reaction process over the time. To confirm this point, the crystal structure and surface electronic states of the silica-modified $InZrO_x$(SCP-4) after reaction for different periods of time are analyzed. Apparently, the diffraction peaks in the XRD patterns, the lattice spacing in the HRTEM images and the binding energies in the In 3*d*, Zr 3*d* and Si 2*p* XPS spectra of the spent $InZrO_x$(SCP-4)-24h and $InZrO_x$(SCP-4)-42h samples are all highly comparable to those of the fresh counterpart (Supplementary Fig. 39j–l and Supplementary Fig. 40a). In addition, the TEM images display that the particle size of $InZrO_x$(SCP-4) is only slightly increased from 6.10 nm of fresh $InZrO_x$(SCP-4) to 6.89 nm of $InZrO_x$(SCP-4)-24h and to 7.30 nm of $InZrO_x$(SCP-4)-42h (Supplementary Fig. 39a–i). Meanwhile, the surface In/Zr and In/Si ratios of $InZrO_x$(SCP-4) also show little change upon the CO_2 hydrogenation reaction test (Supplementary Fig. 40b–e). That is, the major function of the introduced surface silica species is the inhibition of the indium species from reduction and migration in the reductive atmosphere containing hydrogen, whereas without causing any significant structural distortion and atomic rearrangement of the $InZrO_x$ oxide as well as the $InZrO_x$-Beta composite catalyst upon the preparation and reaction process over the time.

Discussion

A composite bifunctional catalyst consisting of $InZrO_x$ oxide and H-Beta zeolite was designed, which exhibits excellent performance in the selective hydrogenation of CO_2 to butane. Under 315 °C, 3.0 MPa, and a space velocity of 1200 mL g^{-1} h^{-1}, a high selectivity of 53.4% to butane in all hydrocarbons (CO free) is achieved at a CO_2 conversion of 20.4% and a selectivity of only about 2% to CH_4.

Various characterization measures and DFT calculation were used to explore the reaction mechanism and structure-performance relationship. The results reveal that the conversion of CO_2 to butane keeps to the tandem methanol-mediated mechanism and the catalytic performance of the $InZrO_x$-Beta composite is related to both the $InZrO_x$ oxide moiety and the H-Beta zeolite moiety. The generation of methanol-related intermediates by CO_2 hydrogenation is closely related to the surface oxygen vacancies of $InZrO_x$, which can be finely tuned through modulating the preparation methods. In contrast, the three-dimensional 12-ring channels of H-Beta zeolite conduces to forming a hydrocarbon pool (HCP) filled with higher methylbenzenes and methylnaphthalenes, which favors the successive transformation of methanol-related intermediates to butane via the aromatic-based cycle, through the alkyl side-chain elimination and subsequent methylation and hydrogenation.

In addition, to tackle the passivation of the acid sites in H-Beta by the migration of indium species of $InZrO_x$ in the reductive atmosphere containing H_2, a surface silica protection strategy was developed, which can effectively inhibit the phase separation of $InZrO_x$ oxide and the indium migration, and then considerably improve the catalytic stability of $InZrO_x$/Beta in the hydrogenation of CO_2 to hydrocarbons. The insight shown in this work may pave a way for the design of stable In-based catalyst in the CO_2 hydrogenation to get a specific hydrocarbon product.

Methods

Catalyst preparation

As described in detail in the Supplementary Information, three $InZrO_x$ oxides with an In/Zr molar ratio of 4 were prepared, viz., $InZrO_x$(CP) by co-precipitation, $InZrO_x$(SG) by sol-gel processing, and $InZrO_x$(HT) by hydrothermal method. In addition, $InZrO_x$(CP) was further modified by depositing 4 and 8 wt.% SiO_2 on the surface, to obtain the SiO_2-modified $InZrO_x$(SCP-4) and $InZrO_x$(SCP-8) oxides, respectively. Meanwhile, a series of H-Beta zeolites with a Si/Al molar ratio (*n*) of 20, 30, 40, 60, and 100 were synthesized by the hydrothermal method and denoted as Beta(*n*). Moreover, H-USY (Si/Al = 5.5) and H-SSZ-13 (Si/Al = 9), purchased from Nankai University Catalyst Co., were used for comparison.

Three manners were used to compose the $InZrO_x$-Beta bifunctional catalysts, viz., dual-bed, granule-mixing, and powder-grinding. By the dual-bed manner, 0.3 g of granule $InZrO_x$ (20–40 mesh) was used as the upper layer and 0.3 g of granule H-Beta (20–40 mesh) as the lower layer. By granule-mixing, 0.3 g of $InZrO_x$ and 0.3 g of H-Beta (both in 20–40 mesh) was mixed in granules. By powder-mixing, 0.3 g of powder $InZrO_x$ and 0.3 g of powder H-Beta were grinded together for 5 min and the powdery mixture was then granulated into particles of 20–40 mesh.

Catalyst characterization

Various catalyst samples were characterized by N_2 sorption, X-ray diffraction (XRD), X-ray photoelectron spectra (XPS), field emission-scanning electron microscopy (FE-SEM), transmission electron microscopy (TEM), high-resolution TEM (HRTEM), Aberration-corrected high-angle annular dark-field scanning TEM (Aberration-corrected HAADF-STEM), temperature-programmed reduction with H_2 (H_2-TPR), temperature-programmed desorption of NH_3 (NH_3-TPD) and CO_2 (CO_2-TPD), thermogravimetric analysis (TGA), inductively coupled plasma-atomic emission spectrometer (ICP-AES), in situ diffuse reflectance infrared Fourier transform (DRIFT) spectroscopy, gas chromatography-

mass spectrometry (GC-MS), and $^{12}C/^{13}C$ methanol switching experiment, as described in detail in the Supplementary Information.

Catalytic reaction tests

The CO_2 hydrogenation reaction was carried out in a stainless steel tubular fixed-bed reactor, as described in detail in the Supplementary Information. Briefly, for the CO_2 hydrogenation to methanol, 0.3 g of $InZrO_x$ was used and the reaction was conducted under 315 °C, 3.0 MPa, and with a space velocity (SV) of 2400 mL g^{-1} h^{-1} and H_2/CO_2 ratio of 3 in the feed. For the CO_2 hydrogenation to butane, unless specially claimed, 0.6 g of granule-mixed bifunctional $InZrO_x$-Beta catalyst (0.3 g $InZrO_x$ + 0.3 g H-Beta) was used and the reaction was performed under 315 °C, 3.0 MPa, a SV of 1200 mL g^{-1} h^{-1}, and H_2/CO_2 ratio of 3 in the feed. For the $InZrO_x$(CP)-Beta composite catalyst prepared by granular mixing, two components of $InZrO_x$(CP) and H-Beta in the spent $InZrO_x$(CP)-Beta catalyst after the reaction test were distinctly different in color, as displayed in Supplementary Fig. 41; therefore, two components can be easily separated by hand according to the granule color, for further characterization. For comparison, the reaction of methanol-to-olefins (MTO) was conducted in a U-type quartz tube loading with 300 mg of H-Beta and with H_2 as the carrier gas, under 315 °C, atmospheric pressure and a methanol weighted hourly space velocity (WHSV) of 0.05 h^{-1}.

DFT calculation

DFT calculation was conducted with the Gaussian 09.E01 package, as described in detail in the Supplementary Information.

Data availability

The source data that support the findings of this study including the article and its Supplementary Information are provided with this paper and are also available in the ScienceDB repository at https://doi.org/10.57760/sciencedb.07972 or available from the author upon reasonable request. Source data are provided with this paper.

References

1. Aresta, M., Dibenedetto, A. & Angelini, A. Catalysis for the valorization of exhaust carbon: from CO_2 to chemicals, materials, and fuels technological use of CO_2. *Chem. Rev.* **114**, 1709–1742 (2014).
2. Dorner, R. W., Hardy, D. R., Williams, F. W. & Willauer, H. D. Heterogeneous catalytic CO_2 conversion to value-added hydrocarbons. *Energy Environ. Sci.* **3**, 884–890 (2010).
3. Porosoff, M. D., Yan, B. & Chen, J. G. Catalytic reduction of CO_2 by H_2 for synthesis of CO, methanol and hydrocarbons: challenges and opportunities. *Energy Environ. Sci.* **9**, 62–73 (2016).
4. Wang, W., Wang, S., Ma, X. & Gong, J. Recent advances in catalytic hydrogenation of carbon dioxide. *Chem. Soc. Rev.* **40**, 3703–3727 (2011).
5. Guo, S. et al. Feasibility, limit, and suitable reaction conditions for the production of alcohols and hydrocarbons from CO and CO_2 through hydrogenation, a thermodynamic consideration. *Ind. Eng. Chem. Res.* **61**, 17027–17038 (2022).
6. Guo, S. et al. Conversion of the CO and CO_2 mixture to alcohols and hydrocarbons by hydrogenation under the influence of the water-gas shift reaction, a thermodynamic consideration. *J. Fuel Chem. Technol.* **51**, 482–491 (2023).
7. Centi, G., Quadrelli, E. A. & Perathoner, S. Catalysis for CO_2 conversion: a key technology for rapid introduction of renewable energy in the value chain of chemical industries. *Energy Environ. Sci.* **6**, 1711–1731 (2013).
8. Jiao, F. & Bao, X. Selective conversion of syngas to light olefins. *Science* **351**, 1065–1068 (2016).
9. Liu, X. et al. Tandem catalysis for hydrogenation of CO and CO_2 to lower olefins with bifunctional catalysts composed of spinel oxide and SAPO-34. *ACS Catal.* **10**, 8303–8314 (2020).
10. Dang, S. et al. Role of zirconium in direct CO_2 hydrogenation to lower olefins on oxide/zeolite bifunctional catalysts. *J. Catal.* **364**, 382–393 (2018).
11. Li, Z. et al. Highly selective conversion of carbon dioxide to lower olefins. *ACS Catal.* **7**, 8544–8548 (2017).
12. Ronda-Lloret, M., Rothenberg, G. & Shiju, N. R. A critical look at direct catalytic hydrogenation of carbon dioxide to olefins. *ChemSusChem* **12**, 3896–3914 (2019).
13. Cui, X. et al. Selective production of aromatics directly from carbon dioxide hydrogenation. *ACS Catal.* **9**, 3866–3876 (2019).
14. Zuo, J. et al. Selective methylation of toluene using CO_2 and H_2 to para-xylene. *Sci. Adv.* **6**, eaba5433 (2020).
15. Ni, Y. et al. Selective conversion of CO_2 and H_2 into aromatics. *Nat. Commun.* **9**, 3457 (2018).
16. Wang, Y. et al. Rationally designing bifunctional catalysts as an efficient strategy to boost CO_2 hydrogenation producing value-added aromatics. *ACS Catal.* **9**, 895–901 (2018).
17. You, Z., Deng, W., Zhang, Q. & Wang, Y. Hydrogenation of carbon dioxide to light olefins over non-supported iron catalyst. *Chin. J. Catal.* **34**, 956–963 (2013).
18. Xu, Y. et al. Selective production of aromatics from CO_2. *Catal. Sci. Technol.* **9**, 593–610 (2019).
19. Wei, J. et al. Precisely regulating brønsted acid sites to promote the synthesis of light aromatics via CO_2 hydrogenation. *Appl. Catal. B* **283**, 119648 (2021).
20. Tu, W. et al. Chemical and structural properties of Na decorated Fe_5C_2-ZnO catalysts during hydrogenation of CO_2 to linear α-olefins. *Appl. Catal. B* **298**, 120567 (2021).
21. Zhang, S. et al. Morphological modulation of Co_2C by surface-adsorbed species for highly effective low-temperature CO_2 reduction. *ACS Catal.* **12**, 8544–8557 (2022).
22. Li, Z. et al. Highly selective conversion of carbon dioxide to aromatics over tandem catalysts. *Joule* **3**, 570–583 (2019).
23. Chen, H. et al. Carbon-confined magnesium hydride nano-lamellae for catalytic hydrogenation of carbon dioxide to lower olefins. *J. Catal.* **379**, 121–128 (2019).
24. Wang, S. et al. Highly effective conversion of CO_2 into light olefins abundant in ethene. *Chem* **8**, 1376–1394 (2022).
25. Wang, S. et al. Selective conversion of CO_2 into propene and butene. *Chem* **6**, 3344–3363 (2020).
26. Liu, Z., Ni, Y., Sun, T., Zhu, W. & Liu, Z. Conversion of CO_2 and H_2 into propane over InZrO and SSZ-13 composite catalyst. *J. Energy Chem.* **54**, 111–117 (2021).
27. Li, Z. et al. Ambient-pressure hydrogenation of CO_2 into long-chain olefins. *Nat. Commun.* **13**, 2396–2405 (2022).
28. Asami, K., Zhang, Q., Li, X., Asaoka, S. & Fujimoto, K. Semi-indirect synthesis of LPG from syngas: conversion of DME into LPG. *Catal. Today* **106**, 247–251 (2005).
29. Fujiwara, M., Satake, T., Shiokawa, K. & Sakurai, H. CO_2 hydrogenation for C_{2+} hydrocarbon synthesis over composite catalyst using surface modified HB zeolite. *Appl. Catal. B* **179**, 37–43 (2015).
30. Li, S., Guo, L. & Ishihara, T. Hydrogenation of CO_2 to methanol over Cu/AlCeO catalyst. *Catal. Today* **339**, 352–361 (2020).
31. Wei, Y. et al. Catalytic roles of In_2O_3 in ZrO_2-based binary oxides for CO_2 hydrogenation to methanol. *Mol. Catal.* **525**, 112354 (2022).
32. Martin, O. et al. Indium oxide as a superior catalyst for methanol synthesis by CO_2 hydrogenation. *Angew. Chem. Int. Ed.* **55**, 6261–6265 (2016).
33. Dang, S. et al. Selective transformation of CO_2 and H_2 into lower olefins over In_2O_3-$ZnZrO_x$/SAPO-34 bifunctional catalysts. *ChemSusChem* **12**, 3582–3591 (2019).
34. Jiang, X. et al. A combined experimental and DFT study of H_2O effect on In_2O_3/ZrO_2 catalyst for CO_2 hydrogenation to methanol. *J. Catal.* **383**, 283–296 (2020).

35. Numpilai, T., Wattanakit, C., Chareonpanich, M., Limtrakul, J. & Witoon, T. Optimization of synthesis condition for CO_2 hydrogenation to light olefins over In_2O_3 admixed with SAPO-34. *Energy Convers. Manag.* **180**, 511–523 (2019).
36. Gao, P. et al. Direct production of lower olefins from CO_2 conversion via bifunctional catalysis. *ACS Catal.* **8**, 571–578 (2017).
37. Frei, M. S. et al. Role of zirconia in indium oxide-catalyzed CO_2 hydrogenation to methanol. *ACS Catal.* **10**, 1133–1145 (2019).
38. Chen, T. et al. Unraveling highly tunable selectivity in CO_2 hydrogenation over bimetallic In-Zr oxide catalysts. *ACS Catal.* **9**, 8785–8797 (2019).
39. Wang, J., Zhang, A., Jiang, X., Song, C. & Guo, X. Highly selective conversion of CO_2 to lower hydrocarbons (C_2-C_4) over bifunctional catalysts composed of In_2O_3-ZrO_2 and zeolite. *J. CO2 Util.* **27**, 81–88 (2018).
40. Wang, W., Chen, Y. & Zhang, M. Facet effect of In_2O_3 for methanol synthesis by CO_2 hydrogenation: A mechanistic and kinetic study. *Surf. Interfaces* **25**, 101244 (2021).
41. Yang, L. et al. Stabilizing the framework of SAPO-34 zeolite toward long-term methanol-to-olefins conversion. *Nat. Commun.* **12**, 4661–4671 (2021).
42. Wang, S. et al. Enhancement of light olefin production in CO_2 hydrogenation over In_2O_3-based oxide and SAPO-34 composite. *J. Catal.* **391**, 459–470 (2020).
43. Gao, P. et al. Direct conversion of CO_2 into liquid fuels with high selectivity over a bifunctional catalyst. *Nat. Chem.* **9**, 1019–1024 (2017).
44. Simonetti, D. A., Ahn, J. H. & Iglesia, E. Mechanistic details of acid-catalyzed reactions and their role in the selective synthesis of triptane and isobutane from dimethyl ether. *J. Catal.* **277**, 173–195 (2011).
45. Wang, Y. et al. Visualizing element migration over bifunctional metal-zeolite catalysts and its impact on catalysis. *Angew. Chem. Int. Ed.* **60**, 17735–17743 (2021).
46. Qi, Y. et al. Photoinduced defect engineering: enhanced photothermal catalytic performance of 2D black In_2O_{3-x} nanosheets with bifunctional oxygen vacancies. *Adv. Mater.* **32**, 1903915 (2020).
47. Zhang, W. et al. Effective conversion of CO_2 into light olefins along with generation of low amounts of CO. *J. Catal.* **413**, 923–933 (2022).
48. Shi, Y. et al. Hierarchically structured Pt/K-Beta zeolites for the catalytic conversion of n-heptane to aromatics. *Microporous Mesoporous Mater.* **324**, 111308 (2021).
49. Ding, H., Zhou, Q., Li, J., Zhu, K. & Fan, W. Self-assembly of silicoaluminophosphate nanocrystals in biphasic media with a water-insoluble structure-directing agent. *Catal. Sci. Technol.* **11**, 5135–5146 (2021).
50. Zhou, C. et al. Highly active ZnO-ZrO_2 aerogels integrated with H-ZSM-5 for aromatics synthesis from carbon dioxide. *ACS Catal.* **10**, 302–310 (2019).
51. Bai, S. et al. Highly active and selective hydrogenation of CO_2 to ethanol by ordered Pd-Cu nanoparticles. *J. Am. Chem. Soc.* **139**, 6827–6830 (2017).
52. Khan, M. U. et al. Pt_3Co octapods as superior catalysts of CO_2 hydrogenation. *Angew. Chem. Int. Ed.* **55**, 9548–9552 (2016).
53. Luo, Y. et al. Conversion of syngas into light olefins over bifunctional ZnCeZrO/SAPO-34 catalysts: regulation of the surface oxygen vacancy concentration and its relation to the catalytic performance. *Catal. Sci. Technol.* **11**, 338–348 (2021).
54. Kattel, S., Yan, B., Yang, Y., Chen, J. G. & Liu, P. Optimizing binding energies of key intermediates for CO_2 hydrogenation to methanol over oxide-supported copper. *J. Am. Chem. Soc.* **138**, 12440–12450 (2016).
55. Wang, C. et al. π-Interactions between cyclic carbocations and aromatics cause zeolite deactivation in methanol-to-hydrocarbon conversion. *Angew. Chem. Int. Ed.* **59**, 7198–7202 (2020).
56. Plessow, P. N., Enss, A. E., Huber, P. & Studt, F. A new mechanistic proposal for the aromatic cycle of the MTO process based on a computational investigation for H-SSZ-13. *Catal. Sci. Technol.* **12**, 3516–3523 (2022).
57. Lesthaeghe, D., Horre, A., Waroquier, M., Marin, G. B. & Van Speybroeck, V. Theoretical insights on methylbenzene side-chain growth in ZSM-5 zeolites for methanol-to-olefin conversion. *Chem. Eur. J.* **15**, 10803–10808 (2009).
58. Zhou, W. et al. New horizon in C1 chemistry: breaking the selectivity limitation in transformation of syngas and hydrogenation of CO_2 into hydrocarbon chemicals and fuels. *Chem. Soc. Rev.* **48**, 3193–3228 (2019).
59. Bao, J., Yang, G., Yoneyama, Y. & Tsubaki, N. Significant advances in C1 catalysis: highly efficient catalysts and catalytic reactions. *ACS Catal.* **9**, 3026–3053 (2019).
60. Su, J. et al. Syngas to light olefins conversion with high olefin/paraffin ratio using $ZnCrO_x$/AlPO-18 bifunctional catalysts. *Nat. Commun.* **10**, 1297 (2019).
61. Ding, Y. et al. Effects of proximity-dependent metal migration on bifunctional composites catalyzed syngas to olefins. *ACS Catal.* **11**, 9729–9737 (2021).

Acknowledgements

The authors sincerely thank to the financial supports of the National Key R&D Program of China (2020YFA0210900; 2018YFB0604802), National Natural Science Foundation of China (U1910203; U1862101; 21991090; 21991092; 22272195; U22A20431), Natural Science Foundation of Shanxi Province of China (202203021224009), Innovation foundation of Institute of Coal Chemistry, Chinese Academy of Sciences (SCJC-DT-2023-06), Youth Innovation Promotion Association CAS (2021172) and Excellent doctoral student award and subsidy program of Shanxi Province (BK2018001).

Author contributions

H.W. and S.F. conducted experiments on catalyst preparation, evaluation, characterization and theoretical calculation; H.W. wrote the paper; S.G. carried out partial catalyst characterization experiments; M.D., H.Z., and W.F. provided some idea and part of the experimental guidance; S.W., Z.Q., and J.W. guided the whole experiments and revised the article; H.W. and S.F. contributed equally to this work. All the authors contributed to the discussions on the experimental and theoretical calculation results.

Competing interests

The authors declare no competing interests.

Additional information

Supplementary information The online version contains supplementary material available at https://doi.org/10.1038/s41467-023-38336-5.

Correspondence and requests for materials should be addressed to Sen Wang, Zhangfeng Qin or Jianguo Wang.

Peer review information *Nature Communications* thanks Hermenegildo Garcia and the other, anonymous, reviewer for their contribution to the peer review of this work. A peer review file is available.